Electrolyte Engineering Stabilizes Photoanodes Decorated with Molecular Catalysts

Ken J. Jenewein,*[a, b] Yuanxing Wang,[c] Tianying Liu,[c] Tara McDonald,[c] Matej Zlatar,[a, b] Nadiia Kulyk,[a] Victoria Benavente Llorente,[a] Attila Kormányos,[a, d] Dunwei Wang,[c] and Serhiy Cherevko*[a]

Molecular catalysts are promising oxygen evolution promoters in conjunction with photoanodes for solar water splitting. Maintaining the stability of both photoabsorber and cocatalyst is still a prime challenge, with many efforts tackling this issue through sophisticated material designs. Such approaches often mask the importance of the electrode-electrolyte interface and overlook easily tunable system parameters, such as the electrolyte environment, to improve efficiency. We provide a systematic study on the activity-stability relationship of a prominent Fe_2O_3 photoanode modified with Ir molecular catalysts using in situ mass spectroscopy. After gaining detailed insights into the dissolution behavior of the Ir cocatalyst, a comprehensive pH study is conducted to probe the impact of the electrolyte on the performance. An inverse trend in Fe and Ir stability is found, with the best activity-stability synergy obtained at pH 9.7. The results bring awareness to the overall photostability and electrolyte engineering when advancing catalysts for solar water splitting.

Introduction

Finding alternative clean energy sources is an ongoing challenge amidst the current energy crisis that faces our fossil fuel-driven society. Solar-based energy conversion utilizes the vast amount of energy stored in the sun to generate clean electricity and thus circumvents environmental pollution by greenhouse gas emissions. Within photoelectrochemical (PEC) cells, solar water splitting occurs by the direct transformation of photon energy into storable chemical bonds (e.g., hydrogen) to address the intermittency of solar radiation. Advancing the oxygen evolution reaction (OER) performance at the photoanode is especially critical due to the sluggishness of the OER,

which acts as a severe bottleneck to the overall efficiency of a PEC water splitting device. A prominent n-type semiconducting photoanode is hematite (α-Fe_2O_3, denoted as Fe_2O_3 from here on).[1] Despite the beneficial characteristics like visible light absorption, low cost, natural abundance, and favorable band alignment for OER, Fe_2O_3 alone greatly underperforms compared to its theoretical maximum solar-to-hydrogen efficiency of 15.4%.[2] This poor efficiency makes it challenging to reach the targeted costs for solar hydrogen of 2.10 \$ $kg_{H_2}^{-1}$ formulated by the United States Department of Energy (DOE).[3] Thus, strategies such as heterojunctions, nanostructuring, electronic modification through doping, or cocatalyst decoration on the surface must be applied to improve hematite-based photoanodes.[4] Within these options, coating with an oxygen evolution catalyst (OEC) to create a hybrid photoelectrode is one of the most popular strategies. Such modifications lead to a reduced recombination rate and faster charge transfer from the photoabsorber to the electrolyte.[5]

Atomically dispersed molecular OECs are a promising material class for constructing hybrid photoelectrodes. In such systems, in contrast to common heterogeneous cocatalysts, single entities of atomic metal catalysts surrounded by a molecular structure are deposited on the photoactive material, retaining the ability of the photoabsorber to fully harness the incident light without any blockage of the light path.[6] Other advantageous features of such molecular catalyst (MC) are the easier identification of reaction mechanisms tied to the well-defined active sites, high atom economy with almost 100% catalyst utilization (i.e., cost-effectiveness), a high degree of tunability by specifically designing the organic ligands, and superior catalytic activity due to the abundant active sites.[7] When two active metal sites are situated in close proximity, the water oxidation mechanism preferentially follows a radical O—O coupling interaction of two metal–oxos (I2 M). The two active sites can either be contained in the same (binuclear) or separate

[a] K. J. Jenewein, M. Zlatar, Dr. N. Kulyk, Dr. V. Benavente Llorente, Dr. A. Kormányos, Dr. S. Cherevko
Helmholtz-Institute Erlangen-Nürnberg for Renewable Energy IEK-11
Forschungszentrum Jülich GmbH
Cauerstrasse 1, 91058 Erlangen (Germany)
E-mail: k.jenewein@fz-juelich.de
s.cherevko@fz-juelich.de

[b] K. J. Jenewein, M. Zlatar
Department of Chemical and Biological Engineering
Friedrich-Alexander-Universität Erlangen-Nürnberg
Egerlandstrasse 3, 91058 Erlangen (Germany)

[c] Dr. Y. Wang, T. Liu, T. McDonald, Prof. Dr. D. Wang
Department of Chemistry, Merkert Chemistry Center
Boston College
2609 Beacon St., Chestnut Hill, MA 02467 (USA)

[d] Dr. A. Kormányos
Department of Physical Chemistry and Materials Science, Interdisciplinary Excellence Centre
University of Szeged
Aradi Square 1, Szeged, H-6720 (Hungary)

ChemSusChem

Research Article
doi.org/10.1002/cssc.202202319

Chemistry
Europe
European Chemical
Societies Publishing

(bimolecular) molecular structure. This pathway requires less overpotential compared to a MC with an isolated single-site character, where OER follows a water nucleophilic attack mechanism. The higher overpotential for this mechanism is needed to produce a sufficiently electrophilic metal-oxo site that facilitates the nucleophilic attack by water. Therefore, designing two active centers situated in close proximity is catalytically more attractive.[8]

Different metal centers, such as Ru[9] or non-noble transition metals,[10] have been demonstrated as active MCs for water splitting. Ir-containing MCs are getting increased attention due to the high OER activity and exceptional stability in aqueous environments known for their oxide form.[11] Recently, OER for Ir MCs has been shown to follow a potential-independent first-order kinetic.[12] On the other hand, IrO_x heterogeneous catalysts exhibit potential-dependent kinetics with cooperative effects between neighboring Ir centers.[13] The absence of such potential dependence for the molecular Ir catalyst was attributed to the specific coordination environment around Ir centers which manifested in higher OER activities at lower overpotentials.[12]

As described earlier, the decoration of the Fe_2O_3 photoanodes with OECs is promising to circumvent their poor PEC performance. Molecular Ir electrocatalysts have been successfully coupled to Fe_2O_3 in previous reports to boost the OER kinetics.[14] For instance, Li et al. have shown that the improvement in OER activity upon deposition of an Ir molecular OEC was mainly due to improved charge transfer, while the surface recombination rate remained unchanged. Therefore, the application of the MCs does not change the surface electronic states of the $Fe_2O_3 | H_2O$ interface.[14a] Similar observations were made by Moir et al. where the decoration of Fe_2O_3 with molecular Ir led to improved OER rates without affecting the flat-band potential and Fermi level pinning. Hence, the effect of the catalyst was mainly of kinetic nature.[14d]

A big challenge when incorporating MCs into photoelectrodes is overcoming the poor stability of the OEC. Assuring good durability of the underlying photoabsorber is equally important since the OEC, assuming intrinsic stability, could be removed from the surface by the degrading photoelectrode underneath.[15] The molecular catalyst must endure harsh oxidative conditions and the presence of reactive oxygen species during OER.[7a] Several decomposition pathways can occur, such as dimerization, oligomerization, and coordination complex reorganization.[16] Organic ligands surrounding the metal center, which help to tune specific catalyst properties, can also become susceptible to oxidative degradation.[7a,14c] Hence, removing the fragile organic ligands from the molecular catalyst by targeted pretreatments can improve stability.[17] In fact, a photochemically treated dinuclear heterogeneous Ir catalyst in conjunction with a Fe_2O_3 photoanode showed good stability under OER conditions at 1.23 V_{RHE} for more than 10 h under near-neutral pH.[14b] Metal oxides present a suitable platform for covalently immobilizing molecular catalysts due to their abundant hydroxyl groups at the surface that can bind strongly to the cocatalyst.[18] Besides the inherent instability of MCs, process-related factors like local pH shifts during OER,
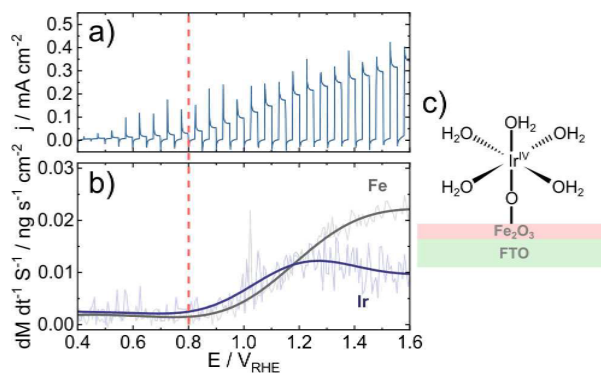
efficient product removal, or charge transfer between the catalyst and semiconductor can all play a decisive role in the stability of the composite photoelectrode. Any insufficiency in these steps can lead to catalyst decomposition due to the accumulation of intermediates or changes in local conditions.[19]

PEC devices must operate for up to 10 years to be commercially viable, as formulated by the DOE.[3] Hence, it is crucial to thoroughly test PEC components for their durability during the early development stages and to understand photo-stability on a fundamental and applied level. Yet, research efforts have mostly focused on improving the activity of PEC materials. Campaigns mapping their long-term stability and efforts to standardize durability tests have only been initiated recently.[20] Especially for hybrid systems with molecular catalysts, detailed degradation studies are scarce. Traditional post-mortem analysis based on physicochemical characterizations only reveal a before/after comparison but does not reveal any details about transformations of the photoelectrode during specific PEC operations.[15a,21] In this light, operando degradation measurements can provide insights into the degradation mechanism of photoelectrodes modified with cocatalysts. In recent years, a photoelectrochemical scanning flow cell coupled to a highly sensitive inductively coupled plasma mass spectrometer (PEC-ICP-MS) has been proven to be a valuable tool for unraveling the in situ photocorrosion processes for state-of-the-art photoanodes such as $BiVO_4$[22] or WO_3.[23]

In this work, we highlight the operando dissolution of a Fe_2O_3 photoanode decorated with a molecular iridium OER catalyst under different PEC protocols. First, the largely disregarded photocorrosion during common PEC performance tests is brought to attention. Then, the in situ dissolution of the cocatalyst-modified photoanode is examined under chronoamperometric holds at different upper potential limits and different time scales. Finally, the influence of pH on the activity-stability relation is investigated. While an in situ dissolution study on Pt single-atom catalysts has been demonstrated for oxygen reduction in the past,[24] the present study marks the first operando degradation survey on photoelectrodes modified with molecular cocatalysts.

Results and Discussion

The photoelectrochemical performance of OEC-decorated photoanodes is often examined by recording the photocurrent during photovoltammograms using chopped illumination. A commonly overlooked process is the catalyst dissolution that already occurs within these short experiments. As similar hybrid photoelectrodes were shown to be highly active and stable under near-neutral conditions,[14b] a 0.05 M $NaNO_3$ electrolyte (pH 5.7) was chosen as starting point for initial investigations. Figure 1a shows the photocurrent density obtained for Fe_2O_3 decorated with an Ir molecular catalyst ($Fe_2O_3 + Ir$-MC) during a photovoltammogram with a shutter frequency of 0.2 Hz. Tracking the in situ dissolution of the Fe species with ICP-MS reveals that $Fe_2O_3 + Ir$-MC shows clear signs of Fe corrosion upon passing 0.8 V_{RHE} (Figure 1b). The onset of dissolution
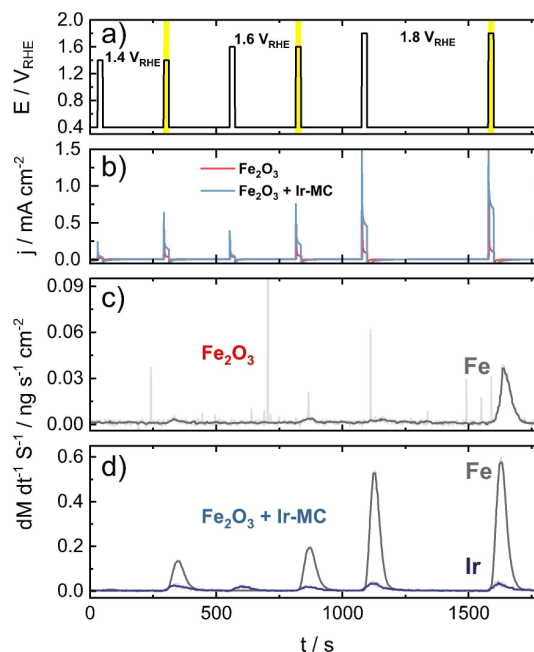
ChemSusChem

Research Article
doi.org/10.1002/cssc.202202319

**Chemistry
Europe**
European Chemical
Societies Publishing

Figure 1. Operando dissolution of Fe_2O_3 + Ir-MC during commonly used PEC screening. a) Photovoltammogram of Fe_2O_3 + Ir-MC recorded in 0.05 м $NaNO_3$ (pH 5.7) under 1 sun AM1.5G illumination, a scan rate of 5 mV s^{-1}, and a shutter frequency of 0.2 Hz. b) In situ dissolution profile of Fe and Ir for Fe_2O_3 + Ir-MC during photovoltammogram measurement. The raw dissolution profiles (lighter color) were smoothed (darker color) using a percentile filter. The dashed line indicates the onset of Fe and Ir dissolution for Fe_2O_3 + Ir-MC. c) Proposed structure of the Ir-MC on Fe_2O_3/FTO.

Figure 2. Dissolution profile of Fe_2O_3 and Fe_2O_3 + Ir-MC during varying chronoamperometric holds under dark/light state and different upper potential limits. a) Applied potential protocol. The yellow bars indicate illumination under 1 sun AM1.5G. b) Resulting current density. c) Dissolution profile of Fe for Fe_2O_3 during PEC protocol in (a). d) Dissolution profile of Fe and Ir for Fe_2O_3 + Ir-MC during PEC protocol in (a). The experiment was conducted in 0.05 м $NaNO_3$ (pH 5.7). The raw dissolution profiles (lighter color) were smoothed (darker color) using a percentile filter.

coincides with the increase in photocurrent density, as highlighted by the dashed line in Figure 1. Ir dissolution follows a similar trend.

To understand the dissolution behavior in more detail, the Fe_2O_3 + Ir-MC sample was subjected to an extended potentiostatic PEC protocol. The experiment consisted of dark and illuminated (1 sun AM1.5G) chronoamperometric (CA) holds at 1.4, 1.6, and 1.8 V_{RHE} as upper potential limits (UPLs). This protocol was designed to reproduce typical operating conditions used by the PEC community. The electrolyte was the same as before, namely 0.05 м $NaNO_3$ (pH 5.7). Additionally, a bare Fe_2O_3 without any cocatalyst was investigated in the same way to evaluate the effect of the Ir-MC on the activity and stability of the photoelectrode. The PEC protocol is illustrated in Figure 2a. As expected, the OEC-loaded photoanode indicates higher photocurrent densities than the one without (Figure 2b), which validates the efficient charge transfer and higher turnover frequency introduced by the molecular catalyst.[14b] The in situ photodegradation for Fe_2O_3 in Figure 2c reveals only negligible Fe dissolution below 1.8 V_{RHE}. CA holds performed in the dark at 1.4 and 1.6 V_{RHE} show no signs of Fe loss, whereas a minor Fe leaching is detected under illumination. A major destabilization is encountered only at an illuminated hold of 1.8 V_{RHE}.
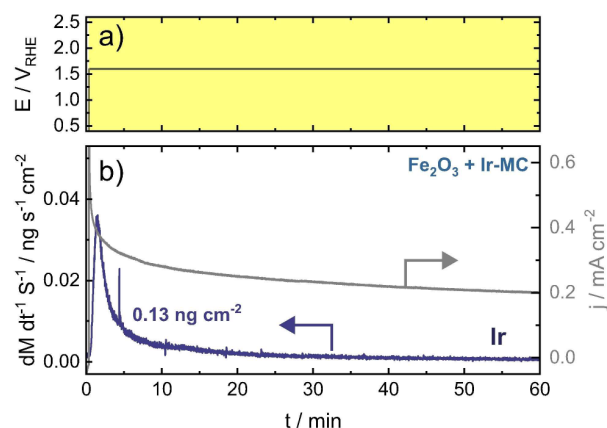
Turning to Fe_2O_3 + Ir-MC, a significantly greater Fe dissolution is observed (Figure 2d). The peak Fe corrosion rate displays an 18-fold increase compared to bare Fe_2O_3. CA holds performed at 1.4 and 1.6 V_{RHE} show a clear distinction in Fe loss during dark and light states. At 1.8 V_{RHE}, however, the Fe dissolution rate of Fe_2O_3 + Ir-MC in the dark and under illumination becomes comparable. It is suggested that at such high potentials, dark OER is majorly triggered, as indicated by the increased anodic current densities reached during the dark 1.8 V_{RHE} hold. Such behavior can contribute to the photoelectrode destabilization. The role of the OER rate on the Fe

dissolution will be highlighted later. The behavior of Ir dissolution rate is less distinctive as illumination does not have an added effect on Ir destabilization. The root of most Ir loss is suspected to be the dissolution of the underlying Fe.

The degradation of molecular catalysts, when used in conjunction with photoelectrodes, is a major bottleneck for its utilization in photoelectrochemistry. Some insights into the Ir loss during PEC operation have been revealed in Figure 2. However, operando dissolution experiments with a scanning flow cell commonly span over a few minutes. Such short time scales only reveal a snapshot of the degradation behavior of the cocatalyst, making it crucial to also record the operando ICP-MS measurements over a longer time frame to gain more detailed insights into the degradation pathway. Hence, the Fe_2O_3 + Ir-MC sample was subjected to a 1 h CA hold at 1.6 V_{RHE}, as shown in Figure 3a, during which the Ir dissolution was tracked simultaneously. As can be seen from Figure 3b, the Ir dissolution rate spikes at the beginning when the potential is ramped up from open circuit potential to 1.6 V_{RHE} and ceases over time during steady-state operation. The total Ir lost during this operation sums to around 0.13 ng cm^{-2}. This observation is contrary to initial expectations of Ir dissolving continuously over time. The instantaneous increase in reaction rate, inflicted by the sudden CA pulse, is most detrimental to the Ir-MC. Observing a time-dependent Ir degradation like this underlines the importance of extended in situ dissolution measurements

ChemSusChem

Research Article
doi.org/10.1002/cssc.202202319

Chemistry
Europe
European Chemical
Societies Publishing

Figure 3. Tracking Ir dissolution for $Fe_2O_3 + Ir$-MC for an extended time at 1.6 V_{RHE}. a) Applied potential protocol. Yellow bar indicates illumination under 1 sun AM1.5G. b) Dissolution profile of Ir for $Fe_2O_3 + Ir$-MC during PEC protocol in (a) and corresponding current density response. The experiment was conducted in 0.05 M $NaNO_3$ (pH 5.7).

with the PEC-ICP-MS setup. Unlike common electrochemical configurations, this system is based on a continuously flowing electrolyte. Therefore, dissolved ions do not accumulate at the electrode surface, which otherwise would influence observations in the transient dissolution due to the gradual approach toward an equilibrium concentration of ions at the vicinity of the electrode.

The steady decrease in Ir loss over time might imply a complete extinction of Ir from the $Fe_2O_3 + Ir$-MC surface. A second, shorter CA hold was performed right after the operation shown in Figure 3a on the same measurement spot to assess this hypothesis. It is expected that if any Ir was still existent on the surface, it would be visible as another increase in Ir dissolution signal. Indeed, the post CA hold verifies the existence of Ir on the photoelectrode surface, evidenced in Figure S1 in the Supporting Information. The total Ir loss during the second hold is around 0.01 ng cm^{-2} and almost one order of magnitude lower than the first hold, which hints toward a depletion of Ir from the surface. To draw conclusions about the fraction of lost Ir during the initial 1 h hold at 1.6 V_{RHE}, a fresh $Fe_2O_3 + Ir$-MC sample was dissolved in concentrated HCl to quantify the amount of Ir per surface area using off-line ICP-MS measurements. This assessment yielded an Ir coverage of 95.14 ng_{Ir} cm^{-2}, translating into an Ir loss of 0.14% during this experiment. X-ray photoelectron spectroscopy (XPS) data recorded before the CA hold indicate the existence of the characteristic Ir^{IV} 4f peaks at 65 eV ($Ir 4f_{5/2}$) and 62 eV ($Ir 4f_{7/2}$) in Figure S2c. The peak positions are in agreement with those found for Ir^{IV} in the surface-bound Ir-MC.[18] After subjection to the prolonged PEC operation, the Ir 4f region diminishes in intensity and the two individual peaks become less distinguishable, which has been shown for similar systems in the past.[14c] The O 1 s and Fe 2p spectra show only a marginal change before and after the 1 h PEC protocol (Figure S2a and b).

With the data from off-line ICP-MS and XPS indicating a significant residue of Ir-MC even after prolonged PEC operations, a second hypothetical decomposition pathway emerges next to Ir depletion. That is, the Ir-MC undergoes a structural reconstruction during the first 1 h CA hold, which seems to have the most destructive consequence in terms of losing Ir. Once transformed, the structurally altered Ir-MC adopts a more stable form and the same potentiostatic hold only causes a smaller Ir loss from the surface. The structural reconstruction could, for instance, be the generation of IrO_x that can form larger aggregated nanoparticles.[16] Such Ir passivation during anodic potentials is expected to be structurally more robust, leading to the observed stabilization of Ir. The morphological change in the Ir-MC is likely responsible for the gradual loss in catalytic efficiency that manifests as the decrease in photocurrent shown in Figure 3b. A useful tool to reveal the Ir state on the photoanode is to perform in situ CO diffuse reflectance infrared Fourier transform, in which Ir nanoparticles show a distinct broad peak at 1850 cm^{-2}, which is absent for the molecular species.[14b] Such measurements could help to uncover whether a structural transformation is happening to the Ir-MC.

After gaining insight into the degradation path of the Ir-MC, the focus returns to the stability of the underlying photoabsober. Unlike Ir, Fe dissolution showed a much clearer dependence on the applied potential, as discussed above for Figure 2. In the past, the self-oxidation by the photogenerated holes has been argued to be a viable degradation mechanism for Fe_2O_3.[25] However, the striking difference in the Fe leaching between Fe_2O_3 and $Fe_2O_3 + Ir$-MC suggests a major contribution from the OER rate. The addition of a cocatalyst drives the oxygen evolution at higher turnover frequencies and thus causes more significant acidification in the vicinity of the photoelectrode. This local pH effect also explains the similarity in Fe leaching at 1.8 V_{RHE} under dark and illuminated states. Since dark OER is majorly triggered, a sufficient proton concentration is generated to render the electrode proximity acidic enough to significantly destabilize Fe, which is also evidenced by the Pourbaix diagram.[26] The nearly absent Fe loss during the dark CA hold at 1.4 and 1.6 V_{RHE} for $Fe_2O_3 + Ir$-MC attests to the fact that dark OER has not yet contributed to corrosion. Suppose the potentiostat would control the current rather than the potential during dark and PEC operation. In that case, the same reaction rate (i.e., similar proton generation) can be expected on the electrode surface. Figure S3 shows the dissolved amount of Fe for $Fe_2O_3 + Ir$-MC during a dark and illuminated chronopotentiometric hold at 1 mA cm^{-2} in a near-neutral electrolyte. The similarity of lost Fe during these two holds suggests that the OER rate is mainly responsible for the differences in the dissolution of Fe.

To corroborate the discussion about the local pH, numerical simulations were performed for a simplified geometric representation of the investigated photoelectrode contacted with the PEC-SFC opening (Figure S4). The calculations reveal that the local proton concentration can differ up to one order of magnitude between a current density of 0.05 mA cm^{-2} ($c(H^+) = 1.16 \cdot 10^{-4}$ M) and 0.4 mA cm^{-2} ($c(H^+) = 9.29 - 10^{-4}$ M) at 1.6 V_{RHE},

ChemSusChem

Research Article
doi.org/10.1002/cssc.202202319

Chemistry Europe
European Chemical
Societies Publishing

which are observed for the bare and Ir-MC-loaded Fe_2O_3, respectively. One order of magnitude difference in proton concentration translates into a pH shift of 1, in which $c(H^+) = 1.16 \cdot 10^{-4}$ M corresponds to pH 3.9 and $c(H^+) = 9.29 \cdot 10^{-4}$ M to pH 2.9. The more substantial decline in local pH for $Fe_2O_3 + Ir$-MC renders the electrode vicinity more acidic, thus making Fe_2O_3 more unstable. The dissolution of Fe_2O_3 at elevated potentials proceeds via Fe^{3+} and becomes potential-independent, as shown by the vertical phase line in the Pourbaix diagram for Fe.[27] The Fe^{3+} concentration then follows Equation (1):

$$\log([Fe^{3+}]) = -0.72 - 3\,pH \tag{1}$$

Equilibrium Fe^{3+} concentrations for pH 3.9 and 2.9 thus significantly vary between $3.8 \cdot 10^{-13}$ M and $2.04 \cdot 10^{-10}$ M, respectively. It is worth noting that Pourbaix calculations are purely based on thermodynamics without considering kinetic considerations.

As shown above, the change in pH can have a detrimental impact on photoelectrode stability. In fact, when undertaking the same extended CA hold shown in Figure 3, but in elevated pH regimes (pH 11.9), a 7-fold increase in the total dissolved amount of Ir is recorded (Figure S5). This result calls for investigating the activity-stability relationship in dependence on pH for $Fe_2O_3 + Ir$-MC. The influence of the pH on the photoelectrochemical properties of Fe_2O_3 has been elucidated in the past.[28] However, a pH study focusing on stability has not been reported for cocatalyst-loaded hematite, and certainly not for hematite decorated with molecular catalysts. Hence, it is appropriate to measure the activity-stability relationship while sweeping the pH of the electrolyte from near-neutral to alkaline. Lower pH values are known to destabilize Fe and are therefore excluded from the following pH study.

Figure 4 shows the recorded photocurrent densities (Figure 4b), Fe (Figure 4c), and Ir (Figure 4d) dissolution rate curves of $Fe_2O_3 + Ir$-MC for a CA hold at 1.4, 1.6, and 1.8 V_{RHE} at three different pH values (5.7, 9.7, 11.9). The photocurrent density gradually increases with more alkaline electrolytes, as is apparent from the summarizing bar chart in Figure 5a. The OER activity of Ir in alkaline is inferior compared to the one in acid.[29] On the other hand, the OER rate of Fe_2O_3 is known to increase when the pH increases due to the mostly deprotonated surface through which OER proceeds via a higher reaction order.[30] Therefore, the contribution from Fe_2O_3 towards the observed photocurrent density in alkaline conditions outweighs the decline in activity of the Ir-MC. This discussion must be held on the premise of assuming 100% Faradaic efficiency, although non-Faradaic currents from self-oxidation cannot be entirely excluded.[16]

A quantitative comparison of the Fe and Ir dissolution across the different pH values and UPLs is highlighted in Figure 5b and c. It is evident that the pH-dependent stability of both elements shows opposite trends. Fe dissolves most at pH 5.7 and almost ceases completely at pH 11.9. This might seem contradictory when juxtaposing these findings with the simplified Pourbaix diagram for Fe in Figure S6a, where Fe is supposedly stable for both pH values. However, the local
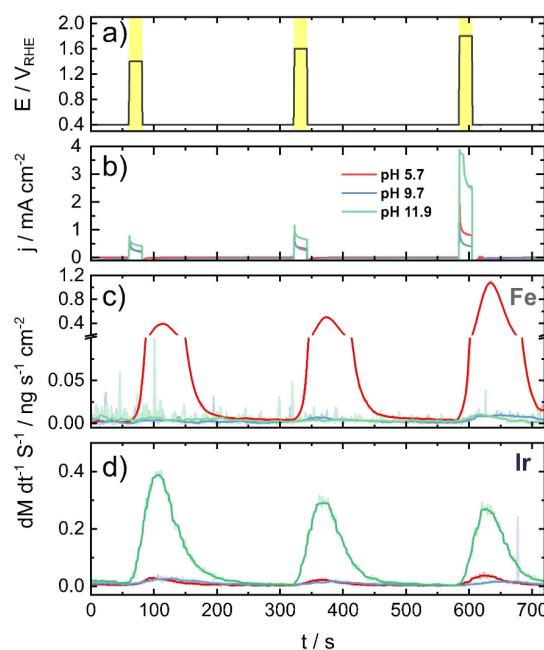
Figure 4. Dissolution profile of Fe and Ir for $Fe_2O_3 + Ir$-MC under varying pH values. a) Applied potential protocol. The yellow bars indicate illumination under 1 sun AM1.5G. b) Resulting photocurrent density. c) Dissolution profile of Fe during PEC protocol in (a). d) Dissolution profile of Ir during PEC protocol in (a). The raw dissolution profiles (lighter color) were smoothed (darker color) using a percentile filter.
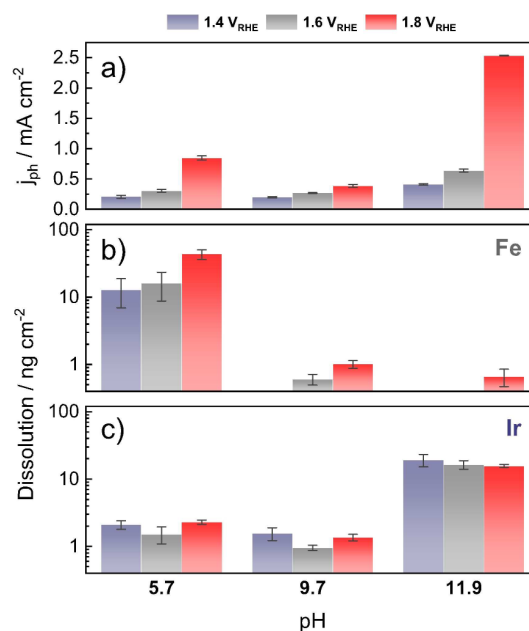
Figure 5. pH study of activity and stability for $Fe_2O_3 + Ir$-MC. a) Photocurrent density during illuminated CAs with different UPLs and pH values. The Photocurrent density was determined by averaging the last 20% of each CA hold lasting 20 s. Total dissolved amount for Fe (b) and Ir (c) during illuminated CAs with different UPLs and pH values. Error bars show the standard deviation of two replicate experiments, and bar graphs mark the mean value.

ChemSusChem

Research Article
doi.org/10.1002/cssc.202202319

Chemistry
Europe
European Chemical
Societies Publishing

acidification through OER is a major issue for unbuffered near-neutral pH values, as discussed above, and is less severe when employing alkaline electrolytes since ubiquitous OH^- ions rapidly neutralize generated protons. Even an incline in pH from 5.7 to 9.7 is enough to suppress the major destabilization of Fe by an order of magnitude. Interestingly, Fe dissolution is completely suppressed when a buffered borate electrolyte (pH 8.7) is used instead of the unbuffered electrolyte at pH 9.7 (Figure S7). The buffered electrolyte is capable of effectively neutralizing protons produced during OER to prevent local pH changes that would harm the hematite photoanode.

Contrary to Fe, Ir dissolves most at pH 11.9. This observation is congruent with past literature[31] and the simplified Pourbaix diagram for Ir in Figure S6b. The inverse trend of dissolved Ir with higher UPLs at pH 11.9 could simply come from the continuous depletion of Ir from the hematite surface or, as described earlier, originate from the transformation into a more stable IrO_x form once the initial structural alteration has taken place. When comparing the Ir dissolution at pH 5.7 and 9.7, it appears that more Ir is lost at pH 5.7. While Ir is more stable at lower pH values, the significant destabilization and loss of Fe could lead to a cooperative dissolution mechanism, in which the extensive Fe corrosion also strips off some Ir-MC. Either Fe or Ir leaching can cause a degradation in the PEC performance. Hence, on-line ICP-MS measurements are essential in understanding which element dissolves under which conditions.

To illustrate the superimposition of the photocurrent density and dissolution data, the charge-normalized total dissolved mols of metals was calculated. The total dissolution represents the sum of observed amounts of Fe and Ir detected with the real-time ICP-MS during the pH study. Normalization by charge incorporates information from the PEC activity into the stability metric, creating a single representation in which a lower value indicates a more stable photoelectrode regardless of whether the stability is achieved by a larger charge or by a smaller metal loss during operation. The summary is depicted in Figure 6, together with the corresponding stability number based on the total number of transferred electrons (S-number (e^-)), which has been introduced as a metric comparing the

activity versus the stability of different (photo)electrocatalysts.[23c,32] The S-number (e^-) follows an inverse relation to the charge-normalized dissolution and is defined as:

$$S-number(e^-) = \frac{n(e^-)}{n(Fe) + n(Ir)} \tag{2}$$

The overall comparison shows that a pH value of 9.7 is the most suitable environment for the $Fe_2O_3 + Ir$-MC out of the ones studied here when considering practically relevant UPLs for PEC applications, namely 1.4 and 1.6 V_{RHE}. In contrast, pH 5.7 creates the most harmful environment as the near-neutral electrolyte is prone to local pH shifts caused by proton generation from OER, which especially destabilizes Fe.[33]

Conclusions

Applying cocatalyst overlayers on hematite is a promising route for enhancing the photoelectrochemical performance. Out of the plethora of catalyst materials, molecular catalysts with active Ir metal centers are an intriguing choice due to their extremely high activity towards oxygen evolution reaction (OER). After unraveling the hidden aspect of Fe and Ir dissolution during commonly used photoelectrochemical (PEC) characterizations, the influence of different operating conditions has been highlighted with the focus on the activity and, more importantly, the operando stability of Fe_2O_3 decorated with a molecular Ir catalyst. Prolonged potentiodynamic holds showed that Ir dissolution is mainly triggered during the sudden initial incline in reaction rate and ceases over time. Off-line inductively coupled plasma mass spectrometry (ICP-MS) and X-ray photoelectron spectroscopy (XPS) results hint toward the formation of a more stable IrO_x as a plausible decomposition path, stabilizing the Ir species. A survey highlighting the influence of the pH demonstrated Fe to be most unstable under near-neutral conditions (pH 5.7), mainly due to local pH shifts coming from OER. The generated protons acidify the vicinity of the photoelectrode, which pushes Fe_2O_3 into a regime of inherent instability. On the other hand, Ir destabilizes with higher pH (pH 11.9). The best synergy between photoactivity and stability was identified at pH 9.7. The effect of a buffered electrolyte on the stability behavior of $Fe_2O_3 + Ir$-MC has been shortly addressed, but more comprehensive investigations have to follow to fully understand the influence of pH buffers on the photostability.

The selection for overlayer materials is often based on band diagrams, Fermi level positions, or the reactivity of the water oxidation catalyst. An equally, if not more important criterion, is the stability of the individual components within a hybrid photoelectrode to ensure high durability of a PEC system. Complex material designs are often applied to remedy intrinsic instability, while the influence of easily adjustable system parameters, like the electrolyte environment, remains largely overlooked and should be considered for novel photoelectrodes for PEC water splitting.
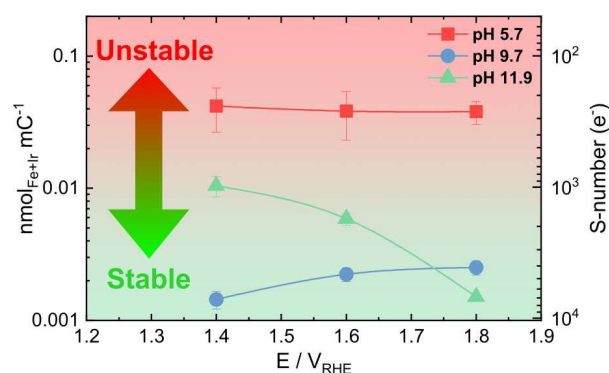
Figure 6. Charge-normalized total dissolution and S-number (e^-) for different pH values and CA holds with increasing UPLs for $Fe_2O_3 + Ir$-MC. Error bars show the standard deviation of two replicate experiments, and points mark the mean value.

Experimental Section

Synthesis of Fe$_2$O$_3$

For the synthesis of hematite, β-FeOOH was deposited on a fluorine-doped tin oxide (FTO) substrate (~7 Ω sq^{-1}, Sigma) in a solution containing 0.15 M iron(III) chloride hexahydrate (FeCl$_3$, 97%, Alfa Aesar) and 1 M sodium nitrate (NaNO$_3$, 99%, Alfa Aesar). The deposition was carried out at 100°C for 1 h. To convert β-FeOOH into hematite, the electrodes were first rinsed and then annealed in a tube furnace at 800°C for 5 min.[34]

Synthesis of Fe$_2$O$_3$+Ir-MC

For the synthesis of Fe$_2$O$_3$+Ir-MC, the precursor, Cp*Ir[pyalc(OH)] (Cp*: pentamethylcyclopentadienyl, pyalc:2-(2′-pyridyl)-2-propanoate), was synthesized by following a previously reported procedure.[35] Then, 0.024 g of Cp*Ir[pyalc(OH)] was dissolved in 50.0 mL deionized water to form a red solution. The Ir homo-dimer was synthesized by adding 1.07 g of sodium periodate (NaIO$_4$, 99.8%, Sigma) to the solution and stirring for 2 h at room temperature. The hematite substrate was soaked in the blue Ir dimer solution for 16 h and then thoroughly rinsed with deionized water to form the Ir heterogenized catalyst. Then, a photochemical treatment was conducted on the substrate by using a UVO cleaner system (Jelight Company Inc.) equipped with a UV light. The process lasted 40 min to yield Fe$_2$O$_3$+Ir-MC.[14b]

Bulk quantification of Ir in Fe$_2$O$_3$+Ir-MC

The bulk quantification of Ir was performed by dissolving the entire Fe$_2$O$_3$+Ir-MC sample in concentrated hydrochloric acid (30%, Suprapur, VWR) at 100°C into a beaker. The solution containing the dissolved ions was transferred into a 50 mL volumetric flask and diluted up to 50 mL. The solution was diluted 10 times before assessing the Ir content by ICP-MS (Nexion 350X, PerkinElmer). Beakers and volumetric flask were cleaned with aqua regia before use to eliminate any contaminants. The beakers were additionally boiled one time in 1 vol% nitric acid (HNO$_3$) prepared by diluting appropriate amounts of concentrated HNO$_3$ (65%, Suprapur, VWR) in ultrapure water (Milli-Q, Merck Millipore). The Ir quantification was conducted based on a four-point calibration curve (0, 0.5, 1, and 5 μg$_{Ir}$ L^{-1}). ^{187}Re at a concentration of 10 μg$_{Re}$ L^{-1} served as an internal standard to ensure good system performance.

PEC-ICP-MS measurements

A detailed overview of the PEC-ICP-MS setup can be found elsewhere.[23a] The light was generated from a 300 W ozone-free Xe lamp (Newport), which was passed through an AM 1.5G filter (Newport) before getting channeled into the photoelectrochemical scanning flow cell (PEC-SFC) via a liquid light guide (Newport). The light was calibrated at the cell opening to 1 sun (100 mW cm^{-2}) using a reference solar cell (Newport).

The three-electrode configuration on the PEC-SFC was formed by using an Ag/AgCl electrode in 3 M KCl (Metrohm) as the reference, a glassy carbon rod (SIGRADUR G, HTW) as the counter electrode, and the sample as the working electrode. PEC protocols were controlled with a Gamry Ref600 potentiostat. All experiments were performed with 0.05 M NaNO$_3$ (99.99%, Sigma) as supporting electrolyte which was constantly purged with Ar. The pH was adjusted using sodium hydroxide monohydrate (NaOH·H$_2$O, 99.99%, Sigma). A borate buffer was used to compare the dissolution behavior to non-buffered solutions for which a 0.05 M

borate buffer was prepared from boric acid (H$_3$BO$_3$, 99.9999%, Sigma) and 1 M NaOH. Measured potentials were all corrected to the reversible hydrogen electrode (RHE) scale and the surface area of the PEC-SFC (0.059 cm^2) was used to normalize all recorded currents. The flow rate of the electrolyte was set to 3.6 μL s^{-1}.

In situ dissolution signals obtained from the ICP-MS were quantified using a four-point calibration curve (0, 0.5, 1, 5 μg L^{-1}) for Ir and Fe. ^{187}Re and ^{59}Co at a concentration of 50 μg L^{-1} served as an internal standard. The ICP-MS was operated under the dynamic reaction cell mode using methane as cell gas. This ensured the elimination of interferences for ^{56}Fe coming from ^{40}Ar^{16}O$^+$ polyatomic species generated by the plasma.

Numerical simulations

Numerical simulation of the pH variation in the vicinity of the electrode was performed in COMSOL Multiphysics using "Laminar flow" and "Transport of diluted species" interfaces in steady-state regime. A 2D model of a flat 2.2 mm wide channel and 3.11 mm long electrode approximately resembled the PEC-SFC setup. An inlet boundary with an average inflow velocity of 4.28 mm s^{-1} and open outflow boundary were applied. The OER rate parameterized as current density was varied, while the concentration of the species (protons) at the electrode was monitored and converted into pH values.

XPS measurements

The X-ray photoelectron spectroscopy (XPS) measurements were performed by a PHI Quantera II scanning XPS microprobe (Physical Electronics, ULVAC-PHI). The photoelectrode samples were contacted to the sample holder via double-sided copper tape. The spectra were acquired using Al Kα irradiation, and a circular area of 200 μm diameter was irradiated at 50 W and 15 kV. High-resolution scans for C 1 s, Fe 2p$_{3/2}$, and Ir 4f were acquired at 140 eV pass energy with a step size of 0.25 eV. The resulting data was analyzed by CasaXPS (V.2.3.18), using instrument-specific relative sensitivity factors and a binding energy scale calibrated to the adventitious carbon peak at 284.8 eV.

Author contributions

K.J.J. designed and performed the PEC-ICP-MS procedures, XPS measurements, and the evaluation of the obtained data. N.K. conducted the numerical simulations. Y.W., T.M., and T.L. synthesized the photoanode samples. M.Z. assisted the ex-situ ICP-MS measurements. K.J.J. wrote the original draft. All authors reviewed and edited the manuscript and participated in scientific discussions. A.K. and S.C. supervised the experimental work.

Acknowledgements

ChemSusChem

Research Article
doi.org/10.1002/cssc.202202319

**Chemistry
Europe**
European Chemical
Societies Publishing

Conflict of Interest

The authors declare no conflict of interest.

Data Availability Statement

The data that support the findings of this study are available from the corresponding author upon reasonable request.

[1] a) P. Sharma, J. W. Jang, J. S. Lee, *ChemCatChem* **2018**, *11*, 157; b) K. Sivula, F. Le Formal, M. Gratzel, *ChemSusChem* **2011**, *4*, 432.

[2] S. Shen, S. A. Lindley, X. Chen, J. Z. Zhang, *Energy Environ. Sci.* **2016**, *9*, 2744.

[3] G. Segev, J. Kibsgaard, C. Hahn, Z. J. Xu, W.-H. Cheng, T. G. Deutsch, C. Xiang, J. Z. Zhang, L. Hammarström, D. G. Nocera, A. Z. Weber, P. Agbo, T. Hisatomi, F. E. Osterloh, K. Domen, F. F. Abdi, S. Haussener, D. J. Miller, S. Ardo, P. C. McIntyre, T. Hannappel, S. Hu, H. Atwater, J. M. Gregoire, M. Z. Ertem, I. D. Sharp, K.-S. Choi, J. S. Lee, O. Ishitani, J. W. Ager, R. R. Prabhakar, A. T. Bell, S. W. Boettcher, K. Vincent, K. Takanabe, V. Artero, R. Napier, B. R. Cuenya, M. T. M. Koper, R. van de Krol, F. Houle, *J. Phys. D* **2022**, *55*.

[4] W. Yang, R. R. Prabhakar, J. Tan, S. D. Tilley, J. Moon, *Chem. Soc. Rev.* **2019**, *48*, 4979.

[5] J. E. Thorne, S. Li, C. Du, G. Qin, D. Wang, *J. Phys. Chem. Lett.* **2015**, *6*, 4083.

[6] a) K. S. Joya, N. Morlanes, E. Maloney, V. Rodionov, K. Takanabe, *Chem. Commun.* **2015**, *51*, 13481; b) J. M. Spurgeon, J. M. Velazquez, M. T. McDowell, *Phys. Chem. Chem. Phys.* **2014**, *16*, 3623.

[7] a) H.-Y. Liu, C. C. Cody, J. A. Jacob-Dolan, R. H. Crabtree, G. W. Brudvig, *ACS Energy Lett.* **2020**, *5*, 3195; b) M. Wang, Y. Yang, J. Shen, J. Jiang, L. Sun, *Sustain. Energy Fuels* **2017**, *1*, 1641; c) J. He, P. Liu, R. Ran, W. Wang, W. Zhou, Z. Shao, *J. Mater. Chem. A* **2022**, *10*, 6835.

[8] D. W. Shaffer, Y. Xie, J. J. Concepcion, *Chem. Soc. Rev.* **2017**, *46*, 6170.

[9] L. Duan, F. Bozoglian, S. Mandal, B. Stewart, T. Privalov, A. Llobet, L. Sun, *Nat. Chem.* **2012**, *4*, 418.

[10] Z. N. Zahran, Y. Tsubonouchi, E. A. Mohamed, M. Yagi, *ChemSusChem* **2019**, *12*, 1775.

[11] a) J. M. Thomsen, D. L. Huang, R. H. Crabtree, G. W. Brudvig, *Dalton Trans.* **2015**, *44*, 12452; b) R. Brimblecombe, G. C. Dismukes, G. F. Swiegers, L. Spiccia, *Dalton Trans.* **2009**, 9374; c) N. T. Suen, S. F. Hung, Q. Quan, N. Zhang, Y. J. Xu, H. M. Chen, *Chem. Soc. Rev.* **2017**, *46*, 337.

[12] C. Bozal-Ginesta, R. R. Rao, C. A. Mesa, Y. Wang, Y. Zhao, G. Hu, D. Anton-Garcia, I. E. L. Stephens, E. Reisner, G. W. Brudvig, D. Wang, J. R. Durrant, *J. Am. Chem. Soc.* **2022**, *144*, 8454.

[13] a) C. Bozal-Ginesta, R. R. Rao, C. A. Mesa, X. Liu, S. A. J. Hillman, I. E. L. Stephens, J. R. Durrant, *ACS Catal.* **2021**, *11*, 15013; b) G. S. Nahor, P. Hapiot, P. Neta, A. Harriman, *J. Phys. Chem.* **2002**, *95*, 616; c) Z. Pavlovic, C. Ranjan, Q. Gao, M. van Gastel, R. Schlögl, *ACS Catal.* **2016**, *6*, 8098.

[14] a) W. Li, D. He, S. W. Sheehan, Y. He, J. E. Thorne, X. Yao, G. W. Brudvig, D. Wang, *Energy Environ. Sci.* **2016**, *9*, 1794; b) Y. Zhao, K. R. Yang, Z. Wang, X. Yan, S. Cao, Y. Ye, Q. Dong, X. Zhang, J. E. Thorne, L. Jin, K. L.

Materna, A. Trimpalis, H. Bai, S. C. Fakra, X. Zhong, P. Wang, X. Pan, J. Guo, M. Flytzani-Stephanopoulos, G. W. Brudvig, V. S. Batista, D. Wang, *Proc. Natl. Acad. Sci. USA* **2018**, *115*, 2902; c) W. Li, S. W. Sheehan, D. He, Y. He, X. Yao, R. L. Grimm, G. W. Brudvig, D. Wang, *Angew. Chem. Int. Ed.* **2015**, *54*, 11428; d) J. W. Moir, E. V. Sackville, U. Hintermair, G. A. Ozin, *J. Phys. Chem. C* **2016**, *120*, 12999.

[15] a) S. Chen, D. Huang, P. Xu, W. Xue, L. Lei, M. Cheng, R. Wang, X. Liu, R. Deng, *J. Mater. Chem. A* **2020**, *8*, 2286; b) G. F. Samu, C. Janaky, *J. Am. Chem. Soc.* **2020**, *142*, 21595; c) F. Nandjou, S. Haussener, *J. Phys. D* **2017**, *50*.

[16] P. Garrido-Barros, C. Gimbert-Surinach, R. Matheu, X. Sala, A. Llobet, *Chem. Soc. Rev.* **2017**, *46*, 6088.

[17] M. Ledendecker, S. Geiger, K. Hengge, J. Lim, S. Cherevko, A. M. Mingers, D. Göhl, G. V. Fortunato, D. Jalalpoor, F. Schüth, C. Scheu, K. J. J. Mayrhofer, *Nano Res.* **2019**, *12*, 2275.

[18] S. W. Sheehan, J. M. Thomsen, U. Hintermair, R. H. Crabtree, G. W. Brudvig, C. A. Schmuttenmaer, *Nat. Commun.* **2015**, *6*, 6469.

[19] B. Zhang, L. Sun, *Chem. Soc. Rev.* **2019**, *48*, 2216.

[20] S. Vanka, G. Zeng, T. G. Deutsch, F. M. Toma, Z. Mi, *Front. Energy Res.* **2022**, *10*.

[21] Royal Society of Chemistry, J. Eichhorn, G. Liu, F. M. Toma, in *Integrated Solar Fuel Generators*, **2018**, pp. 281.

[22] a) S. Y. Zhang, M. Rohloff, O. Kasian, A. M. Mingers, K. J. J. Mayrhofer, A. Fischer, C. Scheu, S. Cherevko, *J. Phys. Chem. C* **2019**, *123*, 23410; b) S. Zhang, I. Ahmet, S. H. Kim, O. Kasian, A. M. Mingers, P. Schnell, M. Kolbach, J. Lim, A. Fischer, K. J. J. Mayrhofer, S. Cherevko, B. Gault, R. van de Krol, C. Scheu, *ACS Appl. Energ. Mater.* **2020**, *3*, 9523.

[23] a) K. J. Jenewein, A. Kormányos, J. Knöppel, K. J. J. Mayrhofer, S. Cherevko, *ACS Meas. Sci. Au* **2021**, *1*, 74; b) J. Knöppel, S. Zhang, F. D. Speck, K. J. J. Mayrhofer, C. Scheu, S. Cherevko, *Electrochem. Commun.* **2018**, *96*, 53; c) J. Knöppel, A. Kormányos, B. Mayerhöfer, A. Hofer, M. Bierling, J. Bachmann, S. Thiele, S. Cherevko, *ACS Phys. Chem. Au* **2021**, *1*, 6.

[24] F. D. Speck, M. T. Y. Paul, F. Ruiz-Zepeda, M. Gatalo, H. Kim, H. C. Kwon, K. J. J. Mayrhofer, M. Choi, C. H. Choi, N. Hodnik, S. Cherevko, *J. Am. Chem. Soc.* **2020**, *142*, 15496.

[25] a) T. Imrich, H. Krýsová, M. Neumann-Spallart, J. Krýsa, *J. Electroanal. Chem.* **2021**, *892*; b) J. Krýsa, T. Imrich, Š. Paušová, H. Krýsová, M. Neumann-Spallart, *Catal. Today* **2019**, *335*, 418.

[26] M. Pourbaix, *Atlas of Electrochemical Equilibria in Aqueous Solutions*, NACE International, **1974**.

[27] B. Beverskog, I. Puigdomenech, *Corros. Sci.* **1996**, *38*, 2121.

[28] a) B. Klahr, S. Gimenez, F. Fabregat-Santiago, T. Hamann, J. Bisquert, *J. Am. Chem. Soc.* **2012**, *134*, 4294; b) S. Chatman, P. Zarzycki, K. M. Rosso, *Phys. Chem. Chem. Phys.* **2013**, *15*, 13911; c) K. Asha, V. R. Satsangi, R. Shrivastav, R. Kant, S. Dass, *RSC Adv.* **2020**, *10*, 42256.

[29] a) D. Y. Kuo, J. K. Kawasaki, J. N. Nelson, J. Kloppenburg, G. Hautier, K. M. Shen, D. G. Schlom, J. Suntivich, *J. Am. Chem. Soc.* **2017**, *139*, 3473; b) H. Ooka, T. Yamaguchi, T. Takashima, K. Hashimoto, R. Nakamura, *J. Phys. Chem. C* **2017**, *121*, 17873.

[30] J. Li, W. Wan, C. A. Triana, H. Chen, Y. Zhao, C. K. Mavrokefalos, G. R. Patzke, *Nat. Commun.* **2021**, *12*, 255.

[31] A. Vass, B. Endrodi, G. F. Samu, A. Balog, A. Kormanyos, S. Cherevko, C. Janaky, *ACS Energy Lett.* **2021**, *6*, 3801.

[32] S. Geiger, O. Kasian, M. Ledendecker, E. Pizzutilo, A. M. Mingers, W. T. Fu, O. Diaz-Morales, Z. Z. Li, T. Oellers, L. Fruchter, A. Ludwig, K. J. J. Mayrhofer, M. T. M. Koper, S. Cherevko, *Nat. Catal.* **2018**, *1*, 508.

[33] J. Y. Kim, J.-W. Jang, D. H. Youn, G. Magesh, J. S. Lee, *Adv. Energy Mater.* **2014**, *4*.

[34] J. W. Jang, C. Du, Y. Ye, Y. Lin, X. Yao, J. Thorne, E. Liu, G. McMahon, J. Zhu, A. Javey, J. Guo, D. Wang, *Nat. Commun.* **2015**, *6*, 7447.

[35] J. M. Thomsen, S. W. Sheehan, S. M. Hashmi, J. Campos, U. Hintermair, R. H. Crabtree, G. W. Brudvig, *J. Am. Chem. Soc.* **2014**, *136*, 13826.